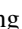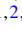# Spin-induced strongly correlated magnetodielectricity, magnetostriction effect, and spin-phonon coupling in helical magnet Fe$_3$(PO$_4$)O$_3$

Arkadeb Pal [1], C. H. Huang,[1] T. W. Yen,[1] P. H. Lee,[1] Y. H. Chang,[1] C. H. Yeh,[1] T. W. Kuo,[1] Ajay Tiwari [1],
D. Chandrasekhar Kakarla [1], S. M. Huang,[1] M. C. Chou,[2] H. S. Kunwar,[3] S. Rana,[3] V. G. Sathe,[3] B. H. Chen,[4]
Y. C. Chuang [4], and H. D. Yang [1,2,*]

[1]*Department of Physics, National Sun Yat-sen University, Kaohsiung 804, Taiwan*
[2]*Center of Crystal Research, National Sun Yat-sen University, Kaohsiung 804, Taiwan*
[3]*UGC-DAE Consortium for Scientific Research, University Campus, Khandwa Road, Indore 452001, India*
[4]*National Synchrotron Radiation Research Center, Hsinchu 30076, Taiwan*

Helical magnets are extremely promising, as they have fascinating magnetic, electric, and phononic properties. Here, we report a spectrum of simultaneously occurring and highly entangled intriguing phenomena induced by helical spin ordering in a noncentrosymmetric and spin-frustrated system Fe$_3$(PO$_4$)O$_3$. These phenomena include magnetodielectric effect in the form of a frequency-independent pronounced dielectric peak, clear magnetostriction effect manifested as a dramatic downturn in the thermal variation of lattice parameters, and strong spin-phonon coupling (which displays a unique anomalous hardening and softening of various phonon modes) at temperatures as high as $T_N = 163$ K. The observed dielectric peak is seemingly associated with a structural distortion via the strong magnetostriction effect.

I. INTRODUCTION

The growing demand for futuristic spintronic devices with enhanced storage capacities and higher energy efficiencies has encouraged research on multifunctional materials that can respond to various external stimuli. These materials display the coexistence of a broad spectrum of intriguing properties that often originate from cross-coupling of several microscopic order parameters such as spins, orbitals, lattices, dipoles, and phonons [1–10]. In this regard, considerable research attention has been devoted to the discovery of new multiferroic and magnetodielectric materials, which largely help in envisaging many real-world applications [1–3,11]. To gain further insight into the relationship with magnetism, the magnetodielectric effect has been studied in various classes of magnetic systems [7,12,13]. Interestingly, recent studies have shown that the dielectric property can effectively characterize intriguing phenomena, such as magnetic quantum criticality and multipole orders [7,8]. However, the number of these materials is scarce because their magnetic and electric properties have mutually antagonistic origins. Although complex noncollinear and noncoplanar spin ordering can lead to ferroelectric ordering, they typically occur at very low temperatures (<40 K) [14]. This low critical temperature limits its practical application. Thus, tailoring such materials with high critical temperatures remains an open challenge. To date, only a few compounds, such as CuO ($T_C \sim 230$ K) and some hexaferrites, have displayed such coupled properties at considerably high temperatures [15–17].

Spin-phonon coupling (SPC), which arises from entangled spin and phonon degrees of freedom, is a fascinating phenomenon in the field of strongly correlated systems [4–6,9], wherein magnetic and structural phase transformations are often reflected in their phonon spectra, and SPC can be facilitated as a fine gauge for monitoring various exotic properties, such as magnetoelectric (ME) coupling, the spin Seebeck effect, the magnetostriction effect, the phonon Hall effect, spin-Peierls transition, and the thermal Hall effect in multiferroics [4,9,18,19].

Crystals without space inversion symmetry can trigger a number of interesting phenomena, including spontaneous electrical polarization, that is, ferroelectricity, the piezoelectric effect, second-harmonic generation (nonlinear optical process), and the linear electro-optic effect [5,20,21]. A geometrically spin-frustrated lattice in such noncentrosymmetric (NCS) crystals adds more advantages by demonstrating complex commensurate and/or incommensurate antiferromagnetic (AFM) ordering, which has attracted intense research attention globally as a promising candidate in the emerging fields of terahertz and subterahertz magnonics and AFM spintronics [22,23]. NCS crystals showing helical AFM ordering are of special interest because of their varied intriguing functionalities, such as voltage-driven switchable spin helicity, spin-driven ferroelectricity, their potential for hosting skyrmions or solitons, and nonreciprocal directional dichroism [5,21,24].

In this regard, the compound Fe$_3$(PO$_4$)O$_3$ (FPO), known as mineral grattarolaite, may be of particular interest [25–31]. Previously, this compound was thought to be ordered in a commensurate collinear AFM phase [31]. Later, using neutron powder diffraction (NPD), Ross *et al.* [27] and Tarne *et al.* [28] showed that FPO develops a highly anisotropic AFM
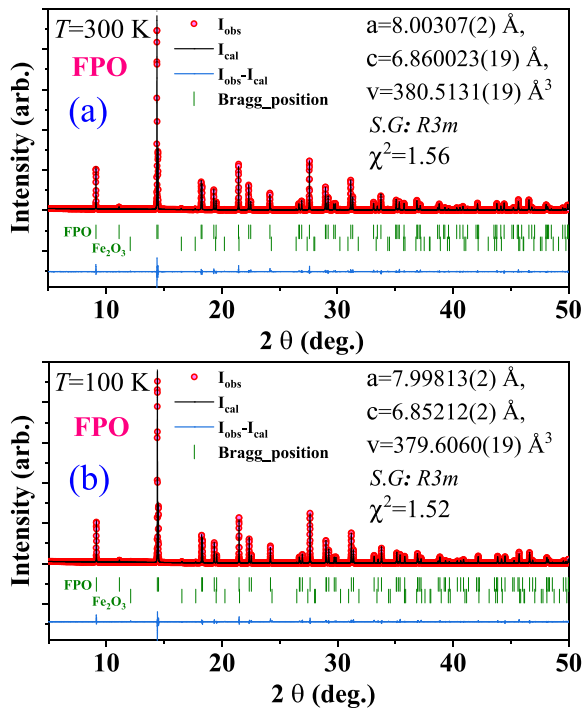
*Corresponding author: yang@mail.nsysu.edu.tw

FIG. 1. Synchrotron x-ray diffraction (SXRD) patterns along with their Rietveld refinements at (a) $T = 300\,K$ and (b) $T = 100\,K$. The green vertical bars indicate the Bragg positions for FPO and Fe_2O_3. The red circles denote the experimental SXRD data, whereas the black line refers to the calculated profile from the Rietveld refinement of the data.

helical spin structure (with domains having a needlelike correlation volume along the hexagonal c axis) below $T_N \sim 163\,K$. Later, Sobolev *et al.* [30] further verified the helical magnetic ordering using Mössbauer spectroscopy. Recently, a single-crystal neutron diffraction study of FPO suggested a special partial helical ordering with a wave vector having a well-defined magnitude but no preferred direction [29], which is like the well-known B20 material MnSi [32]. In contrast to the extensively studied magnetic properties of FPO, a comprehensive study deciphering its dielectric, structural, and phononic properties is hitherto unreported. Nevertheless, owing to its spin-frustrated NCS structure and complex helical AFM magnetic ordering at an appreciably high temperature $T_N \sim 163\,K$, FPO can be a unique playground to study a plethora of intriguing properties, including several strongly correlated phenomena such as the magnetodielectric and/or ME effect, SPC, and the magnetostriction effect.

II. EXPERIMENTAL AND COMPUTATIONAL METHODS

Polycrystalline samples of FPO and $Fe_{2.75}Ga_{0.25}(PO_4)O_3$ were synthesized following a two-step solid-state reaction method, as described elsewhere [30]. In the reactions, dried high-purity ($>99.99\%$, Alfa-Aesar) oxide powders of Fe_2O_3, Ga_2O_3, $FeC_2O_4 \cdot 2H_2O$, and $NH_4H_2PO_4$ were used as initial reagents in a stoichiometric ratio. The final products were initially checked for phase purity by collecting powder x-ray diffraction (XRD) data using a D8 Advance Bruker diffractometer (Cu-$K\alpha_1$, $\lambda = 1.54184\,\text{Å}$). The XRD patterns

at 300 K for both samples are shown in Fig. S1 in the Supplemental Material (SM) [33]. The temperature (T)-dependent synchrotron XRD (SXRD) patterns were recorded at the Taiwan Photon Source 19A beamline of the National Synchrotron Radiation Research Center, Taiwan, with an x-ray wavelength of $0.77489\,\text{Å}$ and a step angle of $0.004°$. To verify the phase and obtain several structural parameters, we performed a Rietveld analysis of both the XRD and SXRD data using the FULLPROF Suite program. The magnetization measurements were performed using a commercial superconducting quantum interference device-based magnetometer (MPMS, Quantum Design). Various dielectric measurements were carried out using a precision Agilent E4980A LCR meter with a helium-based closed-cycle-refrigerator (without a magnetic field) and a commercial Quantum Design MPMS with a homemade dielectric probe (under different magnetic fields). The pyrocurrent data were collected using a Keithley 6517A electrometer in a physical property measurement system (PPMS, Quantum Design). A Horiba Jobin Yvon HR-800 spectrometer equipped with an 1800 g/mm grating, an edge filter for Rayleigh line rejection, and a charge-coupled device detector was employed to record the Raman scattering data. A He-Ne laser (633 nm) beam focused onto a $\sim 2\,\mu m$ diameter spot was used as the excitation source. The data were recorded in the backscattering geometry. The T-dependent Raman

TABLE I. The Wyckoff positions and other structural parameters as obtained from the Rietveld refinement of the SXRD data at 300 and 100 K.

Space group: $R3m$

| Parameters	$T = 300\,K$	$T = 100\,K$
a (Å)	8.00307(2)	7.99813(2)
b (Å)	8.00307(2)	7.99813(2)
c (Å)	6.860023(19)	6.85212(2)
V (Å^3)	380.3131(19)	379.6060(19)
α	90.00	90.00
β	90.00	90.00
γ	120.00	120.00
Fe		
x	0.79671(4)	0.79663(4)
y	$-0.79671(4)$	0.79663(4)
z	0.74055(2)	0.73915(19)
P		
x	0.00000	0.00000
y	0.00000	0.00000
z	0.00000	0.00000
O1		
x	0.00000	0.00000
y	0.00000	0.00000
z	0.23099(7)	0.2306(7)
O2		
x	0.54058(2)	0.53978(2)
y	$-0.54058(2)$	$-0.53978(2)$
z	0.84214(4)	084339(4)
O3		
x	0.56296(19)	0.56229(19)
y	$-0.56296(19)$	$-0.56229(19)$
z	0.27146(18)	0.27062(17)
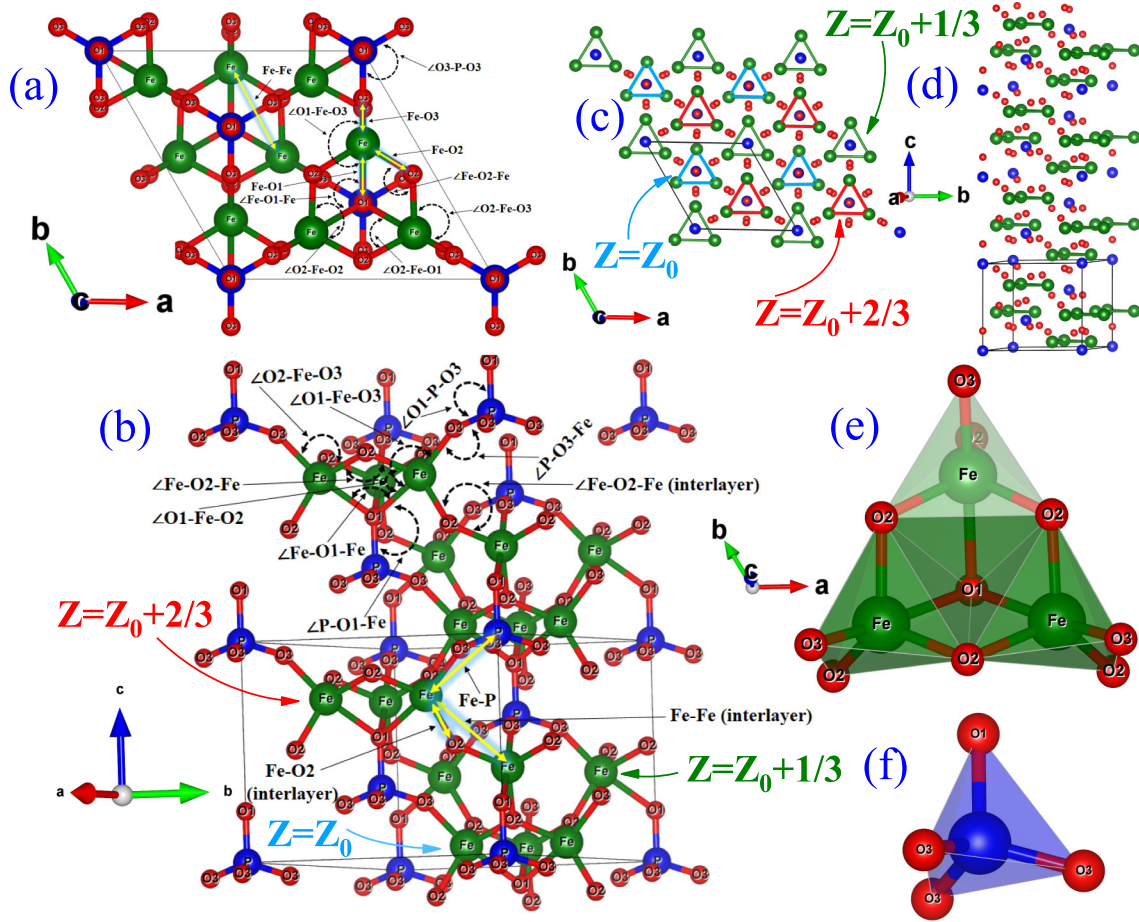
FIG. 2. (a)–(d) Pictorial representations of crystal structure of FPO. Green, blue, and red spheres, respectively, indicate Fe, P, and O atoms. Various bonds and bond angles among different atoms are demonstrated in (a) the FPO crystal structure viewed on the *ab* plane and (b) the crystal structure along the *c* axis. (c) The triangular Fe layers are illustrated as viewed on the *ab* plane, where blue, green, and red triangles are, respectively, forming the bottom ($z = z_0 = 0.07567$), middle ($z = z_0 + \frac{1}{3}$), and top ($z = z_0 + \frac{2}{3}$) layers in a unit cell. (d) Different layers of such coplanar triangular units are stacked along the hexagonal *c* axis. (e) A single triangular Fe unit, which is made up of three edge-shared distorted bipyramids of FeO$_5$, wherein the nearest path between the Fe atoms is formed by joining them via three O(2) atoms, thus forming a coplanar Fe-O(2)-Fe network, whereas the three FeO$_5$ bipyramids share a common O(1) atom, where the bond Fe-O(1) is larger than Fe-O(2). (g) A tetrahedral of PO$_4$.

measurements were carried out using a THMS600 stage from Linkam, U.K. with a temperature stability of ±0.1 K.

The phonon calculations were performed using the density functional perturbation theory via IBRION = 8. Further, the Bilbao Crystallographic Server and a RAMAN-SC package were used for subsequent Raman mode assignments and analysis. The input file for the Raman mode assignments was generated by the first-principles numerical calculations on FPO, using the Vienna *Ab initio* Simulation Package (VASP) version 6.1.2. The details of the calculations are discussed in the SM [33].

III. RESULTS AND DISCUSSION

A. Crystal structure

The calculated Rietveld profiles along with their experimental SXRD patterns collected at 300 and 100 K are depicted in Figs. 1(a) and 1(b), respectively. All the data were satisfactorily fitted with an NCS structure having a trigonal space group $R3m$, thus agreeing with earlier NPD results [27]. A very small ($\sim$1 wt.%) impurity phase of Fe$_2$O$_3$, also reported in earlier studies [27,28], was found in the SXRD data, which was unavoidable during sample preparation. The refined crystallographic parameters (for SXRD at $T = 300$ and 100 K), such as the lattice parameters and Wyckoff positions, are summarized in Table I. The schematic representations of the crystal structure of FPO are demonstrated in Fig. 2. The structure is made up of coplanar triangular units of Fe atoms on the hexagonal *ab* plane.

B. Magnetic properties

Here, T dependence of magnetization (M) curves following the standard zero-field-cooling (ZFC) and field-cooling (FC) protocols were measured under a magnetic field (H) of 1 T, as shown in Fig. 3(a). Shoulderlike broad features followed by sharp drops are observed in both the ZFC and FC branches of the $M(T)$ curves, which are consistent with earlier
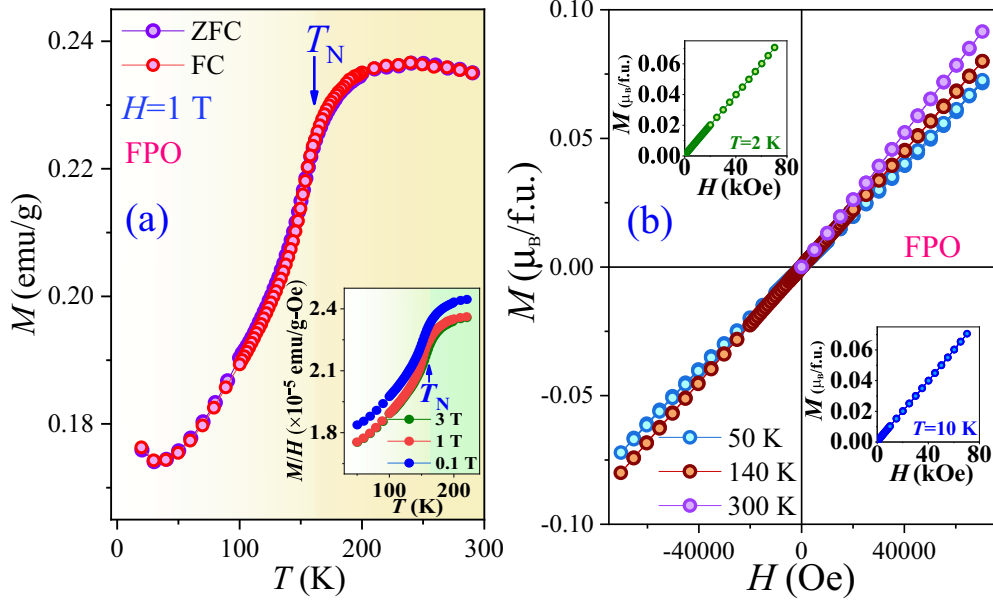
FIG. 3. (a) Zero-field-cooled (ZFC) and field-cooled (FC) $M(T)$ curves at $H = 1$ T. Inset: ZFC $M(T)$ curves at $H = 3.0$, 1.0, and 0.1 T. (b) $M(H)$ curves at $T = 50$, 140, and 300 K. Inset (top): $M(H)$ curve at $T = 2$ K. Inset (bottom): $M(H)$ curve at $T = 10$ K.

reports [27,28]. The observed sharp magnetization drop below $T_N = 163$ K indicates the onset of long-range AFM helical ordering in FPO, as previously confirmed by an NPD study [27,28]. No significant bifurcation was observed between the ZFC and the FC branches. The small increase in M at low-T values may be attributed to the presence of orphan spins associated with lattice defects. The inset of Fig. 3(a) shows the ZFC $M(T)$ curves recorded under various fields $H = 0.1$, 1.0, and 3.0 T. No discernible changes in the position, shape, and pattern of these $M(T)$ curves were observed, suggesting the robust nature of the helical magnetic ordering in FPO under magnetic fields. As demonstrated in Fig. 3(b) and its insets, the nonhysteretic and nonsaturated linear behaviors of the isothermal magnetization curves, that is, the $M(H)$ curves at various T, clearly indicate the AFM nature of the system. Moreover, a short-range correlation among Fe spins prevails above T_N, which leads to a broad shoulderlike feature in the $M(T)$ curve, thereby violating the Curie-Weiss (CW) law [27].

C. Dielectric properties: High-temperature magnetodielectric effect

The NCS crystal structure, along with its complex helical magnetic ordering, renders FPO an interesting system for studying its dielectric and magnetodielectric properties. The thermal variation in the real part of the dielectric constant (ε') at various frequencies (f) with $H = 0$ T is shown in Fig. 4(a). Interestingly, we observed the appearance of singularities in $\varepsilon'(T)$ curves in the form of sharp and well-defined λ-like peaks positioned in the vicinity of T_N, suggesting a magnetodielectric effect. The peak positions were f invariant, whereas the peak strengths were f dependent over a broad f range studied (1–1000 kHz). Moreover, for the entire T range of the study, the observation of the insignificantly small value (<0.009) of the associated dielectric loss (tanδ) sug-

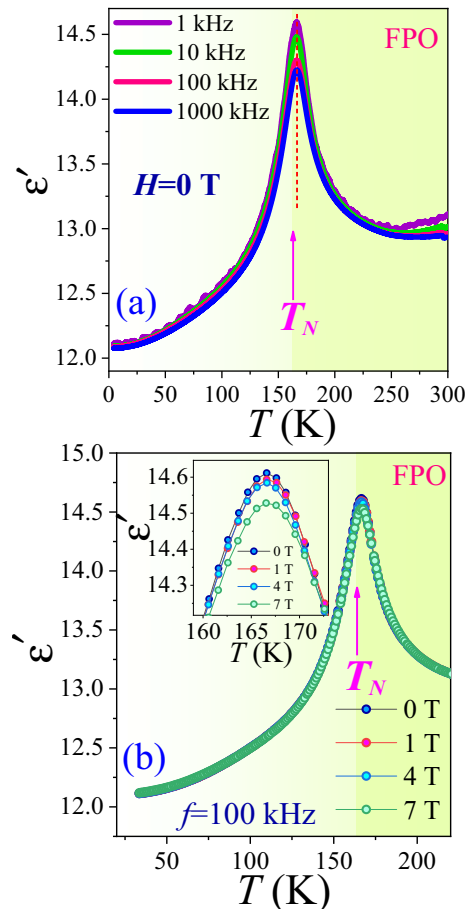FIG. 4. (a) $\varepsilon'(T)$ curves at various f under $H = 0$ T. (b) $\varepsilon'(T)$ curves at $f = 100$ kHz and at different H. Inset: A close view in the vicinity of T_N reveals a weak but clear H dependence of $\varepsilon'(T)$ peaks.

gests the highly insulating nature of FPO, thus ruling out any interference from the extrinsic charge carriers or spurious experimental effects to ε'. All these features of $\varepsilon'(T)$ curves indicate that the underlying origin is not associated with any relaxation phenomenon [20,34]. To further probe the correlation between the magnetic and dielectric properties, we recorded $\varepsilon'(T)$ curves at $f = 100$ kHz under various magnetic fields, as shown in Fig. 4(b). The $\varepsilon'(T)$ curves were not largely affected by the magnetic fields; however, a small but sizeable decrease in $\varepsilon'(T)$ with increasing H was still discernible below T_N, as shown in the inset of Fig. 4(b). In fact, the weak H dependence of $\varepsilon'(T)$ curves tracks the robustness of the spin structure under magnetic fields. An absent or minimal H dependence of $\varepsilon'(T)$ curves is not rare in spin-induced multiferroic systems with robust incommensurate spin structures under magnetic fields [35,36]. Moreover, a similar observation of the weak magnetic field dependence of the dielectric peak induced by a magnetostructural coupling or spin-lattice coupling was also reported in other compounds [37]. For the present system FPO, we also observed a clear structural distortion associated with a magnetostriction effect occurring in the vicinity of its T_N, which apparently gives rise to the observed dielectric peak (which will be discussed later). In this case, an application of magnetic field may not cause a significant change in the structural distortion via the magnetostructural coupling, as the spin structure of FPO seems to be robust with changing H. This may be an underlying plausible reason for the observed weak H dependence of the dielectric peak in FPO.

To further validate the magnetic origin of the dielectric peak, we studied the nonmagnetic dilution effect (i.e., by partially replacing Fe^{3+} with Ga^{3+} ions in FPO) on the dielectric properties of the isostructural hybrid system $Fe_{2.75}Ga_{0.25}(PO_4)O_3$. According to the reported NPD results, $Fe_{2.75}Ga_{0.25}(PO_4)O_3$ exhibits long-range helical spin ordering at $T_N = 118$ K. The $\varepsilon'(T)$ curves at various frequencies (under $H = 0$ T) along with the $M(T)$ curve of $Fe_{2.75}Ga_{0.25}(PO_4)O_3$ are shown in Fig. S2 in the SM [33]. Interestingly, clear dielectric peaks (with their positions not varying with frequencies) near $T \sim 120$ K were observed for the $Fe_{2.75}Ga_{0.25}PO_4O_3$ system. Hence, this undoubtedly confirms that the underlying helical spin ordering indeed plays a pivotal role in originating the dielectric peaks in the FPO and $Fe_{2.75}Ga_{0.25}PO_4O_3$ systems, thus referring to a marked correlation between the magnetic and dielectric properties, i.e., a magnetodielectric effect. Furthermore, pyrocurrent (I_p) measurements were performed, displaying peaks in two opposite directions for opposite poling, which started appearing above T_N (as described in Fig. S3 in the SM [33]). Although the signal shows noisy and broader peaks, it consistently showed similar results after checking multiple times on different pieces of samples. This may indicate the occurrence of weak electric polarization associated with a possible weak ME coupling near the T_N. Generally, at such a high temperature, thermally stimulated free charge carriers largely dominate the intrinsic pyrocurrent of a system, which may be one possible reason for the lack of a clear I_p signal for FPO if a small electric polarization is truly present. Moreover, the absence of a comprehensible I_p signal may be related to the polycrystalline nature of the sample, as such results have been reported in other ME systems

[38]. However, further experimental and theoretical studies are required to provide unambiguous proof. Nevertheless, the observation of the spin-induced strong and sharp dielectric peaks (indicating a prominent magnetodielectric effect) at such a high temperature ($T_N \sim 163$ K) eventually places FPO among the extremely rare materials.

In fact, magnetodielectric and multiferroic ME properties have been reported in a number of systems, including helical magnets, in which the magnetostriction effect arising from helical magnetic ordering plays a key role in evoking such coupled phenomena [21,36,39]. Similarly, for the present helical magnet FPO, the observed dielectric peak appears to be originated from a structural distortion mediated by a magnetostriction effect, which is clearly unraveled in the T-dependent SXRD study (discussed in the following section).

D. T-dependent SXRD: Magnetostriction effect

To investigate the evolution of the crystal structure of FPO with T, particularly in the vicinity of its T_N, we plotted the thermal variations of the refined lattice parameters, that is, a, c, and unit-cell volume (V), as shown in Figs. 5(a)–5(c), respectively. Interestingly, all the lattice parameters exhibited clear anomalies by demonstrating sudden downturn features near $T_N = 163$ K, as evident in Fig. 5. Concomitant sudden changes in the Bragg reflections of the T-dependent SXRD patterns were distinctly observed near T_N, which is visible in the color-coded contour plot of SXRD, as shown in the inset of Fig. 5(a) (for the most intense peak) and Fig. S5 in the SM [33]. For the entire temperature range studied, neither peak splitting in an existing Bragg reflection nor the apparition of an additional Bragg peak in the SXRD patterns was observed (Figs. S4 and S5 in the SM [33]). This rules out the possibility of a global crystal symmetry change. Therefore, the anomalous thermal variations of the lattice parameters near T_N appear to be related to a structural distortion induced by the magnetostriction effect, which arises due to a cross-coupling between the spin ordering and the lattice.

Furthermore, the magnetostriction effect can be probed by investigating the thermal expansion of various lattice parameters, which solely involves elastic degrees of freedom. Generally, for a system, the thermal variations of its lattice parameters associated with thermal expansion [40] follow the equations expressed as follows: $a(T) = a_0\{1 + \frac{B\exp(d/T)}{T[\exp(d/T)-1]^2}\}$; $c(T) = c_0\{1 + \frac{f\exp(g/T)}{T[\exp(g/T)-1]^2}\}$; and $V(T) = V_0\{1 + \frac{A}{[\exp(\theta_D/T)-1]}\}$; where a_0, c_0, and V_0 are the lattice constants at $T = 0$ K, and B, d, f, g, and A are the adjustable fitting parameters. Here, θ_D is the Debye temperature. It is evident from Fig. 5 that, for the entire T range (300–100 K), all three lattice parameters, a, c, and V, could not be fitted with the above equations in a single curve fitting. Instead, the fit was satisfactory when fitted separately in two different T regions, that is, above and below T_N, as demonstrated in Fig. 5. The fitted parameters are summarized in Table SI in the SM [33]. These observations essentially suggest that the magnetostriction effect results in an altered thermal expansion behavior of the lattice parameters below T_N (due to the rise of various exchange interactions as the strong magnetic correlation develops) and concomitantly leads to a substantial structural distortion in the lattice. However, if the spontaneous
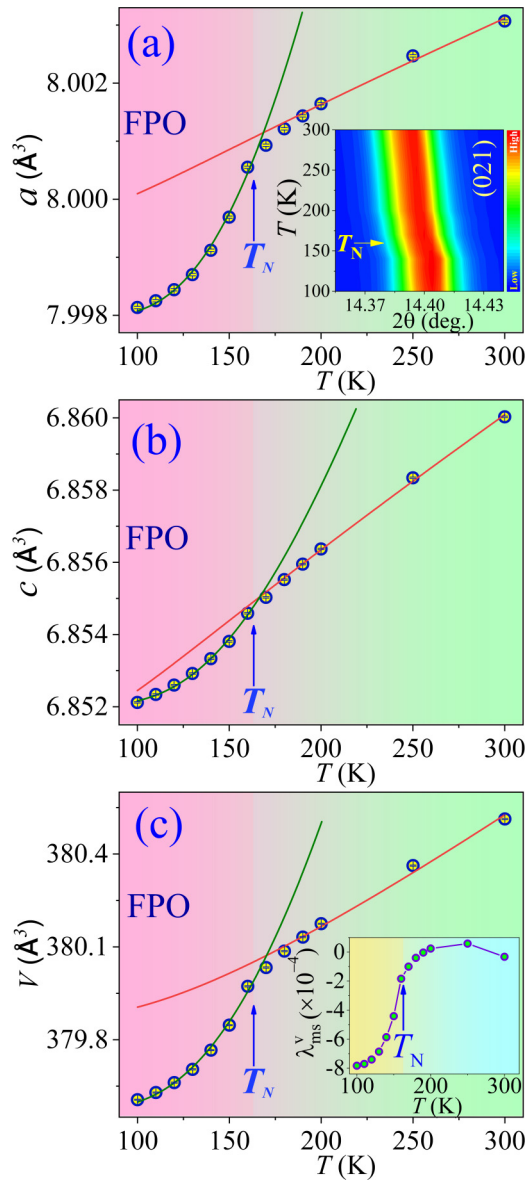
FIG. 5. (a)–(c) T variations of the unit-cell lattice parameters, i.e., a, c, and volume (V) as derived from T-dependent synchrotron x-ray diffraction (SXRD) pattern analysis. The solid red and green lines represent the thermal expansion fit of the curves in the regions $T > T_N$ and $T < T_N$, respectively. Due to the occurrence of a magnetostriction effect, the thermal expansion behavior of various lattice parameters showed a drastic change near T_N. Inset of (a): The corresponding sudden change in the peak position [for (021) Bragg reflection] near T_N observed in the color-coded contour plot of SXRD as a function of T and 2θ (deg.). Inset of (c): T variation of volume magnetostriction.

lattice distortion (maintaining the global crystal structure) due to the magnetic ordering is sufficiently large, the resulting spontaneous magnetostriction effect can be quantitatively estimated using the SXRD data, which is also advantageous over other conventional capacitive and strain-gauge techniques [41,42]. The spontaneous volume magnetostriction (λ_{ms}^{V}) at a certain T can be determined by considering the difference between the volume of a system in an ordered magnetic state

[such as ferromagnetic (FM) and AFM] and that in a paramagnetic (PM) state [43], such that $\lambda_{ms}^{V}(T) = \frac{V_{AFM}(T) - V_{PM}(T)}{V_{PM}(T)}$, where $V_{AFM}(T)$ denotes the actual V in the AFM state at temperature T, and $V_{PM}(T)$ represents the V of the system in a hypothetical situation, where the system is in a PM state at the same T. For FPO, the T variation of λ_{ms}^{V}, as calculated from its V vs T curve, is shown in the inset of Fig. 5(c). The $\lambda_{ms}^{V}(T)$ curve exhibits a sharp drop near T_N and follows a pattern very close to the $M(T)$ curve, as shown in Fig. 3(a), thus suggesting a close correspondence between the magnetic and lattice degrees of freedom in FPO. At $T = 100$ K, the value of λ_{ms}^{V} is $\sim 7.8 \times 10^{-4}$, which is comparable with the previously reported values of the spontaneous volume magnetostriction found in the spinel compounds $Zn_{1-x}Cu_xCr_2Se_4$ ($\lambda_{ms}^{V} \sim 4.6 \times 10^{-4}$ to 24.9×10^{-4} at 100 K for different values of x) and in the $15R$-type hexagonal $BaMnO_3$ compound ($\sim 32 \times 10^{-4}$ at 90 K) [4,43]. Therefore, the estimated large value of λ_{ms}^{V} indicates the presence of a substantial magnetostriction effect in the FPO system.

It is relevant to mention here that the magnetic ordering in FPO is established via various magnetic exchange interactions occurring among different triangular Fe units [Fig. 2(c)], which is formed by joining three edge-shared distorted bipyramids of FeO_5 clusters [as shown in Fig. 2(e)]. Inside an individual triangular Fe unit, the exchange interactions occur via Fe-O(2)-Fe and Fe-O(1)-Fe pathways. In its three-dimensional magnetic sublattice, different coplanar (on the ab plane) triangular Fe units are connected to each other by PO_4 units, i.e., via the weaker exchange pathways Fe-O(3)-P-O(3)-Fe [as shown in Fig. 2(b)]. On the other hand, the interplane triangular Fe units (for two successive layers) are connected via the Fe-O(2)-Fe paths, thus providing a strong interlayer exchange interactions path. Thus, in case the structural distortion occurs via a magnetostructural coupling, it may be interesting to investigate the thermal variations of various bonds and bond angles involved in these exchange interactions among the triangular Fe units [i.e., clusters of FeO_5 bipyramids consisting of atoms Fe, O(1), O(2), and (O3)]. Hence, to get a deeper insight into the structural evolution, we further analyzed various microscopic structural parameters [as indicated in Figs. 2(a) and 2(b)] at different T and show their T variation in Fig. 6 (only for the parameters related to an individual triangular Fe unit) and Fig. S6 in the SM [33] (for some other parameters). Interestingly, clear anomalies are observed for all the studied parameters near T_N, thus suggesting an occurrence of a structural distortion in the clusters of FeO_5 bipyramids forming the triangular Fe units. For FPO, the position of the P atom remains unaffected and fixed at (0 0 0) at all temperatures. Thus, the anomalies observed in the parameters related to the PO_4 tetrahedra are solely due to the variations in O(1) and (O3), which are also included in the FeO_5 clusters and thus participating in the various magnetic exchange interactions, as mentioned above. Thus, the observed structural distortion associated with the triangular Fe units (i.e., the FeO_5 clusters) seems to be closely interlinked with the magnetic ordering via a magnetostructural coupling. Moreover, the underlying possible origin of the dielectric anomaly near T_N is seemingly embedded in the observed structural distortion via the magnetostructural coupling or magnetostriction effect.
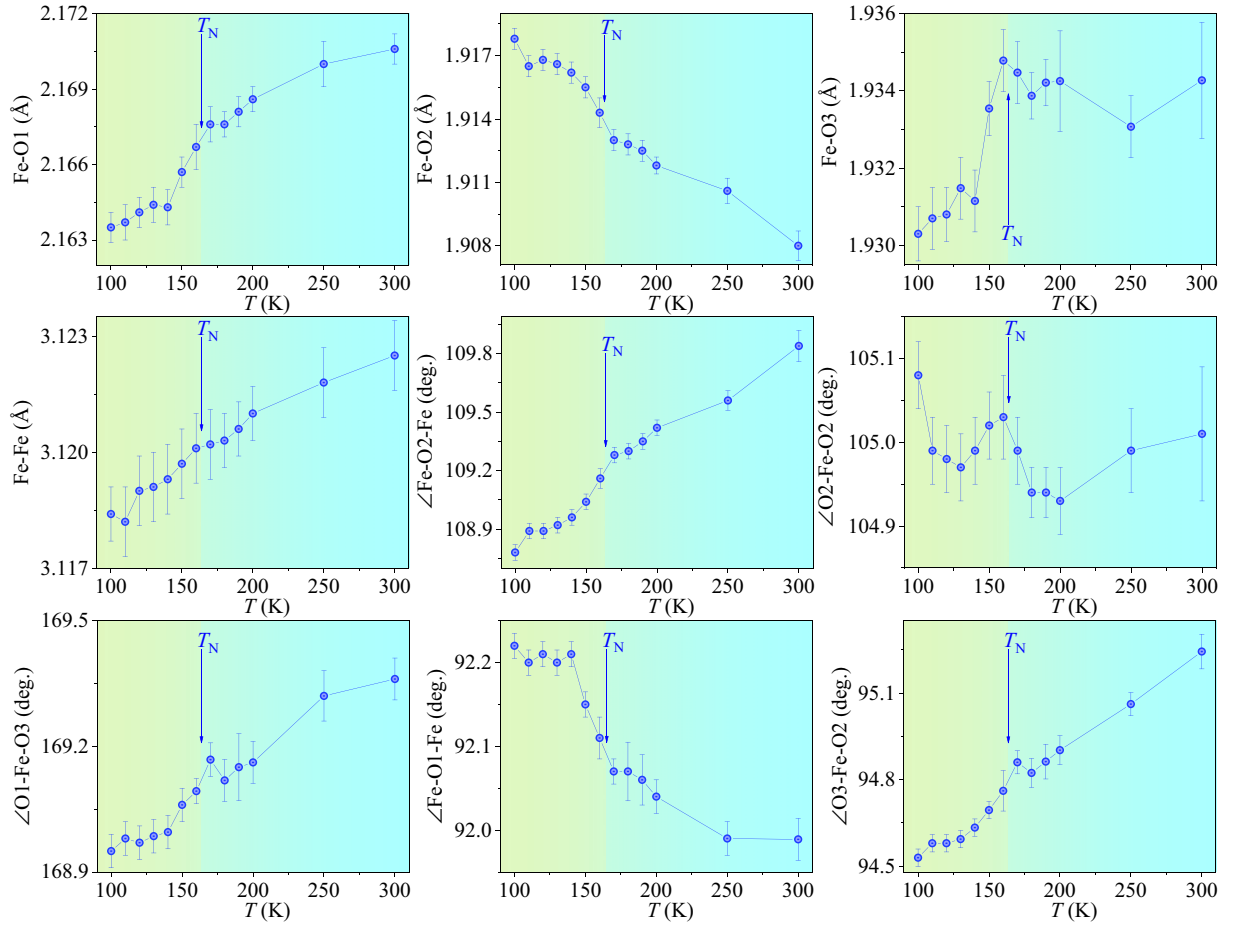
FIG. 6. Thermal variations of several bonds and bond angles related to an individual triangular Fe unit. The observed clear anomalies near T_N for all the parameters indicate the occurrence of a structural distortion in the triangular Fe unit, which is formed by the clusters of FeO_5 bipyramids.

E. T-dependent Raman spectroscopy: Strong SPC

A number of helical magnetic systems were reported to host intriguing phenomena, which are related to inherently coupled spin, lattice, and phonon degrees of freedom [5,6,44]. This prompted us to study the lattice dynamics of FPO further by investigating its T-dependent Raman spectra. Unlike diffraction techniques, which can probe the global structure of a crystal, Raman spectroscopy provides a unique and powerful gauge which can sense local structural change, SPC, cationic ordering, etc. The group theoretical symmetry analysis of FPO with trigonal space group $R3m$ (No. 160; point group C_{3v}) predicted that there could be 22 modes, including 17 simultaneously active Raman ($7A_1 + 10E$) and infrared ($7A_1 + 10E$) modes, two acoustic modes ($A_1 + E$), and three additional hyper-Raman active modes ($3A_2$) at the Γ-point of the Brillouin zone. Here, each E symmetry represents a doubly degenerate mode. Raman spectra of FPO collected at various temperatures are shown in Fig. 7(a). Enlarged views of different sections of the spectra are displayed in Figs. 7(b)–7(d), where the designations of various observed Raman modes are shown as P1–P16. The symmetry assignments of the various modes were performed by calculating the phonon spectrum using density functional theory calculations,

the Bilbao Crystallographic Server, and the PHONOPY program [45]. The details of the possible origins of these different Raman modes along with their symmetry assignments are summarized in Table SII in the SM [33].

Color-coded contour plots of the Raman peak intensities as a function of T and phonon excitation frequency (ω) are shown in Fig. S7 in the SM [33]. A clear sign of anomalous hardening or softening near T_N was observed for several Raman modes, as shown in Fig. S7 in the SM [33], which appears to be the indication of an underlying SPC and magnetostriction in FPO. Thus, for a comprehensive understanding of the observed anomalous phonon behavior, we analyzed the thermal evolution of the peaks using Lorentzian fitting. The variations of ω as a function of T for all the observed Raman modes (except P8, which did not show systematic T variation) are shown in Fig. 8, while the associated full width at half maxima or line-width (Γ) variations are depicted in Fig. S8 in the SM [33]. Generally, for a material with magnetic ions, the T variation of ω can be expressed as $\omega(T) = \omega_0 + \Delta\omega_{\text{latt}}(T) + \Delta\omega_{\text{anh}}(T) + \Delta\omega_{\text{e-ph}}(T) + \Delta\omega_{\text{s-ph}}(T)$, where ω_0 is the frequency at the initial temperature T_0, $\Delta\omega_{\text{latt}}$ is the contribution from the lattice contraction or expansion, $\Delta\omega_{\text{anh}}$ is the anharmonic contribution, and $\Delta\omega_{\text{e-ph}}$ and $\Delta\omega_{\text{s-ph}}$ are the changes originating from
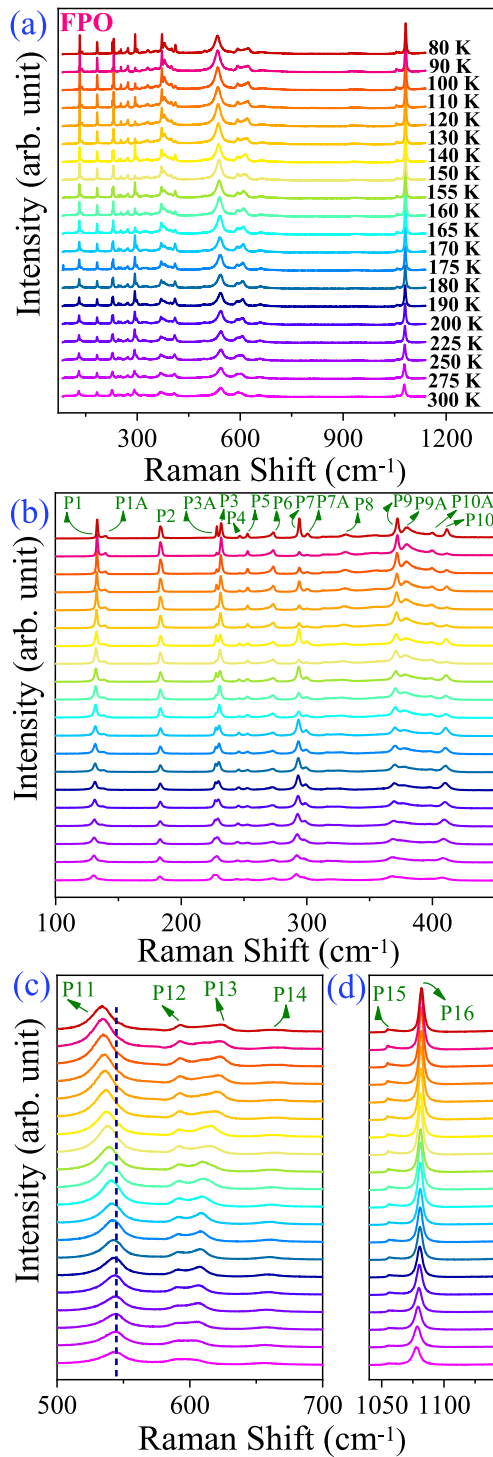
FIG. 7. (a) Raman spectra recorded at various T. (b)–(d) Closer views of the spectra in three different regions. The dashed blue straight line in (c) is a guide to eyes that shows anomalous softening of the P11 mode.

the electron-phonon and SPC, respectively [46]. Thus, in the absence of any structural change, spin-phonon, or electron-phonon coupling, ω follows the typical anharmonic equation [5,9]: $\omega_{\mathrm{anh}}(T) = \omega_0 - C[1 + \frac{2}{\exp(\hbar\omega_0/2k_BT)-1}]$; where C is an adjustable parameter, $\hbar$ represents the reduced Planck's constant, and k_B denotes the Boltzmann's constant. Therefore, the

$\omega(T)$ curves following the anharmonic relation should demonstrate gradual hardening as T decreases, thereby plateauing at a lower T. It is worth noting that, although there exists short-range ordering (SRO) above T_N [which was evidenced from the local maxima in the $M(T)$ curve], for most of the Raman modes, $\omega(T)$ curves do not show phonon renormalization above T_N and thus follow the anharmonic behavior at least down to T_N (Fig. 8). It may essentially suggest that the existing SRO in FPO may not effectively result in a significant phonon modulation via SPC above T_N, i.e., the effect may be minimal or absent for most of the Raman modes. In fact, similar anharmonic behavior of various phonon modes in the SRO region above T_N was also reported in other systems, such as Cu_2OCl_2 and Ni_2NbBO_6 [6,47]. However, as the strong spin-correlation develops near T_N, substantial phonon renormalization occurs via SPC for at least eight different modes, P1, P3, P9, P11, P12, P13, P14, and P15, which is manifested as remarkable sharp deviations (in the form of strong anomalous hardening or softening) from the anharmonic curve in the vicinity of T_N, as can be seen in Fig. 8. Similarly, the anharmonic relation followed by the corresponding $\Gamma(T)$ is given as [4]: $\Gamma_{\mathrm{anh}}(T) = \Gamma_0 + A[1 + \frac{2}{\exp(\hbar\omega_0/2k_BT)-1}]$, where A is an adjustable parameter, and Γ_0 denotes Γ at $T \to 0$ K. Deviations from the anharmonicity near T_N were also observed in the $\Gamma(T)$ curves of various modes, as shown in Fig. S8 in the SM [33]. In the present case, the effect of the electron-phonon coupling on the phonon anomaly can be ruled out, as FPO is a highly insulating compound. As already discussed, a strong magnetostriction effect occurred near T_N; thus, the resulting strong structural distortion may essentially play a key role in manifesting such anomalous phonon behavior. In addition, for various modes, the noticeable anomalies in both the $\omega(T)$ and $\Gamma(T)$ curves near T_N further indicate the existence of a direct coupling between spin and phonon in FPO [48]. Generally, $\Gamma(T)$ remains unaffected by the magnetostriction effect; thus, the observed anomaly in $\Gamma(T)$ in FPO signals a change in phonon lifetime around T_N owing to SPC [44]. It can be further noted that, for a few modes, such as P1, P3, P9, and P11, the $\omega(T)$ curves display small but discernible deviation from the anharmonic behavior above T_N. It is apparently associated with a finite phonon renormalization for these modes via a weak SPC due to the existence of SRO. This kind of a sizeable deviation of the $\omega(T)$ curves from the anharmonic nature above T_N was also reported in other systems for a few modes (while the other modes showed usual behavior or got least affected by SRO), which was attributed to the effect of SPC due to the existence of SRO [5,47]. As previously mentioned, the magnetic exchange interactions among the Fe spins in each triangular unit occur via O(1) and O(2), whereas O(3) provides another weaker exchange interaction pathway for the Fe spins residing on two different but neighboring coplanar triangular units. Thus, as spin correlation develops in FPO, it can eventually affect various phonon modes involving these oxygen atoms (that form clusters FeO_5 bipyramids), thus leading to an SPC effect.

Although there are at least eight phonon modes exhibiting large and prominent anomalous deviation near T_N, the P11 mode displayed a unique pattern in $\omega(T)$ variation, which is very similar to the $M(T)$ curve, thus providing a direct shred of evidence for SPC in FPO [as shown in Fig. 9(a)]. The possible reason for the uniqueness of the P11 mode may
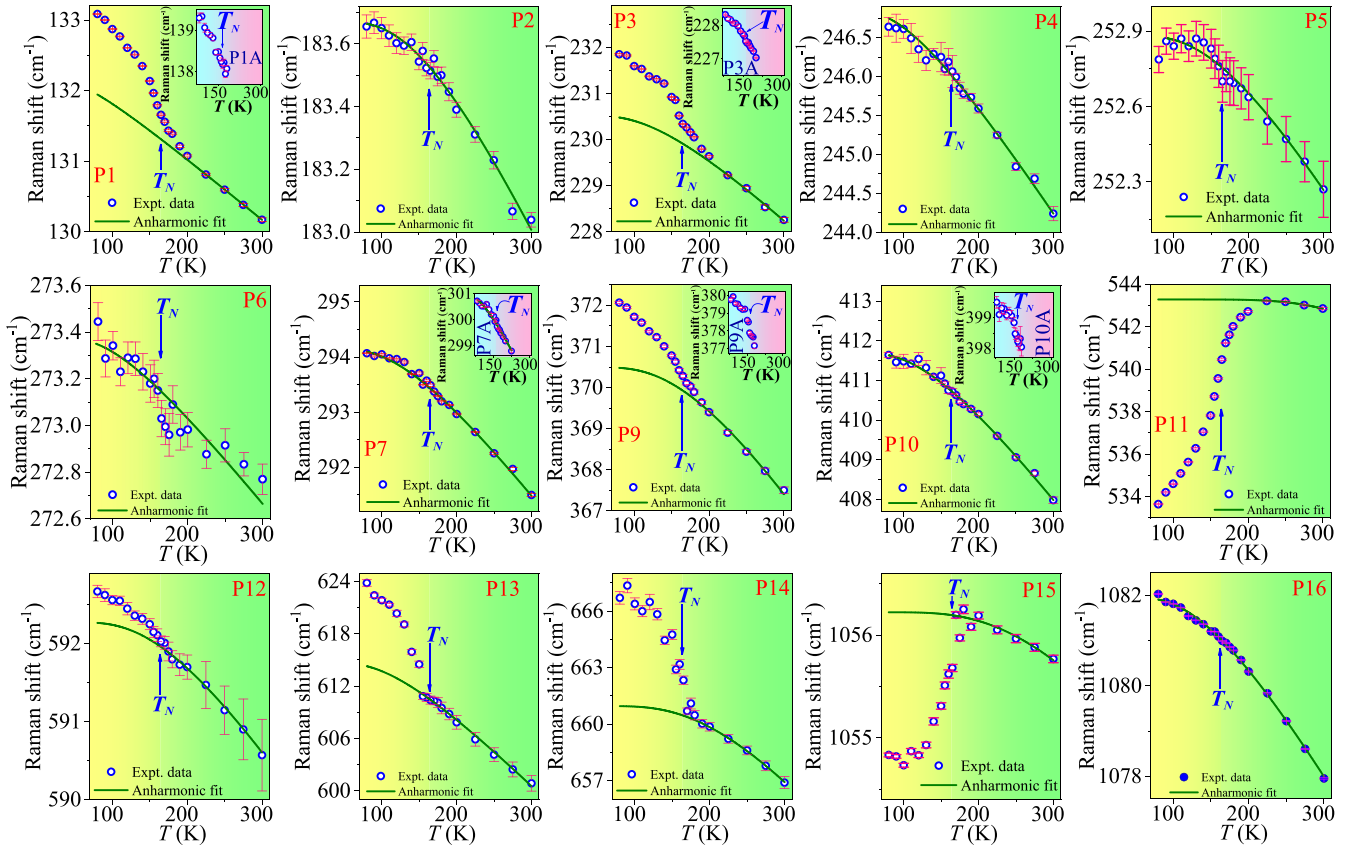
FIG. 8. $\omega(T)$ curves along with the anharmonic fits for various Raman modes of FPO. The deviation of $\omega(T)$ curves from anharmonic law near T_N is a manifestation of the combined effect of spin-phonon coupling (SPC) and magnetostriction. Insets: $\omega(T)$ curves for new Raman modes originated from the peak splitting due to magnetostriction.

be related to its underlying symmetric breathing vibration of the Fe-O(2)-Fe bonds [as depicted in the inset of Fig. 9(a)]. In a triangular Fe unit, Fe-O(2)-Fe provides the shortest exchange interaction path [as Fe-O(1) > Fe-(O2)] between two Fe spins. Thus, as magnetic correlation develops, it may have more close correlation with the P11 mode, thus manifesting as the unique pattern in its $\omega(T)$ curve, which may be particularly interesting. Surprisingly, the thermal variations of three solely different parameters (which were obtained from SXRD, dc magnetization, and Raman spectroscopy measurements): λ_{ms}^{V}, M, and ω (for P11), were closely matched with each other by following similar patterns, as is evident from Fig. 9(a). This direct observation undoubtedly confirms the existence of strong mutual coupling among the spin, lattice, and phononic order parameters in FPO. In SPC process, as the spin correlation grows, phonon renormalization occurs through a modulation of the lattice vibration. Based on the formalism proposed by Granado *et al.* [46,49], the coupling between spins and phonons can be expressed as follows: $\Delta\omega_{s\text{-ph}}(T) \approx \lambda\langle\mathbf{S}_i \cdot \mathbf{S}_j\rangle \approx 3\lambda\{\frac{M(T)}{M_{\text{Max}}}\}^2$, where the constant λ is a measure of the strength of the SPC and $\langle\mathbf{S}_i \cdot \mathbf{S}_j\rangle \approx 3\{\frac{M(T)}{M_{\text{Max}}}\}^2$ represents the nearest-neighbor spin-spin correlation function [M_{Max} denotes the value of the maximum magnetization observed in $M(T)$ data]. Factor 3 appears owing to the presence of three nearest-neighbor FM-coupled Fe spins in each triangular unit on the *ab* plane. To avoid complexity, we have

shown the data of $\Delta\omega$ and $\{\frac{M(T)}{M_{\text{Max}}}\}^2$ as a function of T for only the P11 mode in Fig. 9(b), whereas the corresponding data for other modes also showing SPC are shown in Fig. S9 in the SM [33]. Interestingly, for all the modes displaying the anomalous softening or hardening, the two entities of different origins (i.e., phonon and spin) showed similar patterns by displaying anomalies in the vicinity of T_N. This behavior is a typical feature of a system showing SPC, where phonons are modulated near T_N by the magnetic ordering [46,49]. Moreover, according to the formalism of Granado *et al.* [46], for a Raman mode exhibiting SPC, the $\Delta\omega$ vs $\{\frac{M(T)}{M_{\text{Max}}}\}^2$ curve should follow a linear behavior, and the value of λ can be simply estimated from its linear fitting in the long-range ordering region [6,49]. For FPO, the various Raman modes displaying anomalous softening or hardening showed linear variations in $\Delta\omega$ vs $\{\frac{M(T)}{M_{\text{Max}}}\}^2$ plots, which are evident from Fig. 10(a) for the P11 mode and Fig. S10 in the SM [33] for other modes, thus further suggesting the underlying SPC effect. Moreover, the corresponding values of λ for various Raman modes of FPO were obtained from the linear fitting performed in the T range of 165–80 K, which were in the range of -11.77 (hardening) to 8.04 (softening). Such considerably large values of λ suggest the occurrence of a significantly strong SPC in FPO as compared with other magnetic oxide materials, such as CuB_2O_4 ($\lambda \sim 0.02-0.03\,\text{cm}^{-1}$), Sr_2CoO_4 ($\lambda \sim 3.5\,\text{cm}^{-1}$), La_2CoMnO_6 ($\lambda \sim 2.1\,\text{cm}^{-1}$), $Sr_4Ru_3O_{10}$
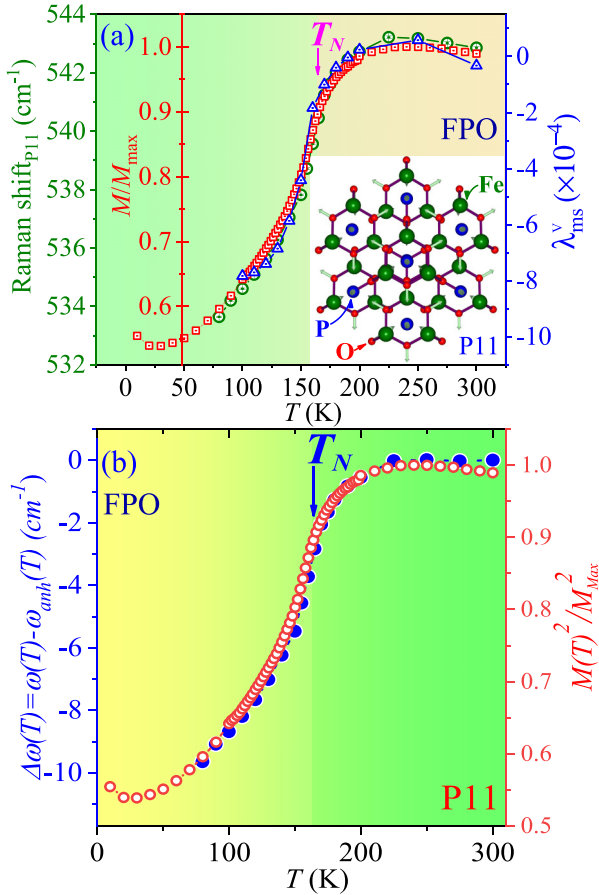
FIG. 9. (a) T variations of ω (for P11 mode), $M/M_{\max}$, and λ_{ms}^{V}; all of them closely follow similar patterns, thus suggesting a strong interplay between various microscopic degrees of freedom, such as spin, lattice, and phonon in FPO. Inset: Pictorial representation of the lattice vibration related to the P11 mode. (b) T variation of $\Delta\omega$ and $\{\frac{M(T)}{M_{\mathrm{Max}}}\}^2$ for the P11 mode. Similar patterns of these curves indicate the underlying spin-phonon coupling (SPC).

FIG. 10. (a) $\Delta\omega$ vs $\{\frac{M(T)}{M_{\mathrm{Max}}}\}^2$ plot for the P11 mode and its linear fits to estimate the spin-phonon coupling (SPC) constant λ. The linear nature of the curve indicates presence of the SPC. (b) Grüneisen law fit to the ($\Delta\omega/\omega$) vs ($\Delta V/V$)) curve for the P11 mode. The linearity of the curve also suggests the existence of a strong correlation between the lattice distortion and phonons.

($\lambda \sim 5.2\,\mathrm{cm}^{-1}$), Ni$_2$InSbO$_6$ ($\lambda = 0.55-2.14\,\mathrm{cm}^{-1}$), and Ni$_2$NbBO$_6$ ($\lambda = -0.3$ to $+0.67$) [5,47,49–52]. On the other hand, the spiral magnet CuO was reported to show an exceptionally strong SPC effect with $\lambda = -50\,\mathrm{cm}^{-1}$ [53].

Following the simplified lattice model proposed by Sushkov *et al.* [54], we further calculated an approximate value of the SPC constant λ for the P11 mode (showing the unique anomalous softening): $\lambda \approx \frac{2\alpha^2 J}{m\omega_0}$, where $\alpha = 2z/3a_B = 6.301\,\text{Å}^{-1}$ (z denotes the nearest-neighbor coordination number of Fe, and a_B is the Bohr radius), and the exchange coupling constant is given by $J = 3k_B\theta_{CW}/zS(S+1) = 5.32\,\mathrm{meV}$; here, k_B is the Boltzmann constant, $\theta_{CW} = 1000\,\mathrm{K}$ denotes the CW temperature (an approximate value reported earlier [27]), $S = \frac{5}{2}$, m = mass of the Fe ion, $\omega_0 = 2(\frac{K0}{m})^{1/2}$ is the mode frequency calculated from the Raman shift. Our calculation yielded a value of $\lambda \approx 5.3\,\mathrm{cm}^{-1}$, which is of the order of the experimentally obtained value of λ.

As previously mentioned, the phonon mode variation $\omega(T)$ also involves a quasiharmonic effect $\Delta\omega_{\mathrm{latt}}$, which arises from the ionic binding energy changes due to the lattice expansion or contraction [46]. Therefore, in addition to the effect of SPC
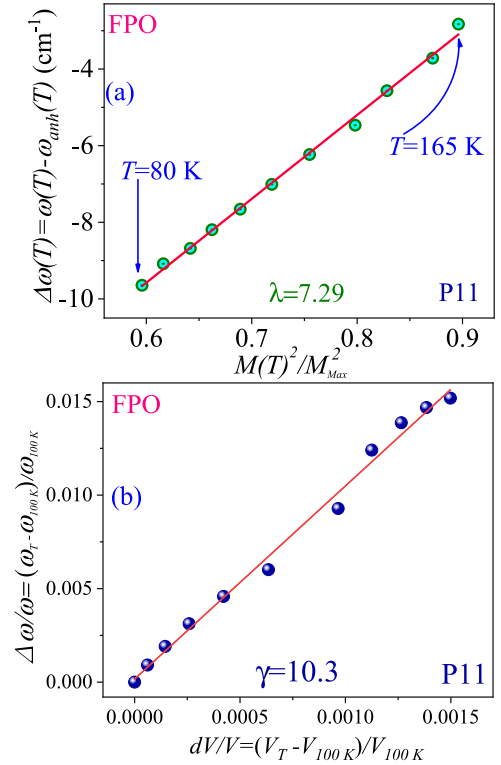
(with a direct coupling between the spin and the phonon) on the phonon modulation in FPO, the observed magnetostriction effect appears to play a crucial role in triggering the anomalous phonon behavior. Typically, the effect of unit-cell volume (V) change on the phonon mode frequency ω can be approximated by Grüneisen's law: $(\frac{\Delta\omega}{\omega}) = -\gamma(\frac{\Delta V}{V})$, where γ is the Grüneisen parameter for a phonon mode [46]. The Grüneisen's law linear fit to the $(\frac{\Delta\omega}{\omega})$ vs $(\frac{\Delta V}{V})$ curves are demonstrated in Fig. 10(b) for the P11 mode and in Fig. S11 in the SM [33] for the other modes. Interestingly, the observed satisfactory linear fit for various Raman modes further attests to the role of the magnetostriction effect as an important contributing factor in modulating the phonon modes. Moreover, a lattice distortion via the magnetostriction effect can lead to new Raman modes or splitting of existing Raman modes due to the emergence of magnetic ordering [4,55]. In the present system, we also detected the appearances of new peaks, P1A, P3A, P7A, P9A, and P10A, which emerged in the form of a shoulder or peak splitting from their respective main peaks [Fig. 7(b)]. These peaks mostly appeared in the temperature regime, where strong short-range spin correlations developed near $T \sim 240\,\mathrm{K}$, and the peak intensities of these modes gained more weight below T_N. Hence, this can be presumably attributed to the enhanced short-range AFM correlation among the Fe spins, which seems to trigger the observed new peaks

via a structural distortion arising due to the magnetostructural coupling or magnetostriction effect. The observed variations in the $\omega(T)$ curves for these new modes are shown in the insets of Fig. 8.

Following the Lyddane-Sachs-Teller relation that provides a direct correspondence between the dielectric constant and optical phonon frequency, the SPC effect was interlinked with the dielectric anomalies in various systems [56–58]. Thus, in addition to the crucial role played by the magnetostriction effect in triggering the dielectric peak (via a structural distortion) in FPO, the observed SPC effect may also be related to the dielectric anomaly in this system. However, detailed studies with polarization-dependent Raman spectra and single-crystal investigations may be required to verify this scenario.

Eventually, the presence of SPC were recently reported on a couple of different helimagnets, such as Cu_2OCl_2 displaying anomalous phonon hardening and Ni_2InSbO_6 showing anomalous phonon softening near their respective T_N [5,6]. However, both anomalous hardening and softening of Raman modes with strong coupling (i.e., high λ) are scarce phenomena, which makes FPO a unique system. Similar interesting observations of phonon hardening and softening of different Raman modes (with intermediate values of λ) were recently reported on an armchair chain compound Ni_2NbBO_6 [47]. Nevertheless, the present observation of the uniquely coupled spin, lattice, phonon, and dipolar properties in FPO can shed new light on understanding the strongly correlated phenomena in such frustrated magnetic systems.

IV. CONCLUSIONS

A spectrum of concurrent strongly correlated intriguing phenomena, including a spin-driven frequency-independent strong dielectric peak manifesting a magnetodielectric effect, a large magnetostriction effect evidenced from an atypical downturn feature in the T dependence of lattice parameters, and a unique and strong multimode SPC (in the form of both anomalous phonon hardening and softening) were observed in the vicinity of a helical AFM magnetic ordering at a temperature as high as $T_N = 163$ K in a NCS spin-frustrated magnet $Fe_3(PO_4)O_3$ (FPO), thus placing it among extremely rare materials. The crucial role of the large magnetostriction effect in driving the phonon anomalies was validated by Grüneisen's law analysis. Further, a linear variation of $\Delta\omega$ vs $\{\frac{M(T)}{M_{Max}}\}^2$ curve confirmed the presence of SPC. Such a large magnetostriction effect leading to a strong structural distortion seems to be the key factor for emanating the observed magnetodielectric effect in FPO.

[1] W. Eerenstein, N. D. Mathur, and J. F. Scott, Multiferroic and magnetoelectric materials, Nature (London) **442**, 759 (2006).

[2] D. Khomskii, Classifying multiferroics: Mechanisms and effects, Physics **2**, 20 (2009).

[3] S.-W. Cheong and M. Mostovoy, Multiferroics: A magnetic twist for ferroelectricity, Nat. Mater. **6**, 13 (2007).

[4] B. Poojitha, A. Rathore, A. Kumar, and S. Saha, Signatures of magnetostriction and spin-phonon coupling in magnetoelectric hexagonal 15*R*-BaMnO$_3$, Phys. Rev. B **102**, 134436 (2020).

[5] M. A. Prosnikov, A. N. Smirnov, V. Y. Davydov, Y. Araki, T. Arima, and R. V. Pisarev, Lattice and magnetic dynamics in the polar, chiral, and incommensurate antiferromagnet Ni_2InSbO_6, Phys. Rev. B **100**, 144417 (2019).

[6] B. S. Araújo, A. M. Arévalo-López, J. P. Attfield, C. W. A. Paschoal, and A. P. Ayala, Spin-phonon coupling in melanothallite Cu_2OCl_2, Appl. Phys. Lett. **113**, 222901 (2018).

[7] J. W. Kim, S. Khim, S. H. Chun, Y. Jo, L. Balicas, H. T. Yi, S.-W. Cheong, N. Harrison, C. D. Batista, J. Hoon Han *et al.*, Manifestation of magnetic quantum fluctuations in the dielectric properties of a multiferroic, Nat. Commun. **5**, 4419 (2014).

[8] K. Kimura, P. Babkevich, M. Sera, M. Toyoda, K. Yamauchi, G. S. Tucker, J. Martius, T. Fennell, P. Manuel, D. D. Khalyavin *et al.*, Magnetodielectric detection of magnetic quadrupole order in $Ba(TiO)Cu_4(PO_4)_4$ with Cu_4O_{12} square cupolas, Nat. Commun. **7**, 13039 (2016).

[9] A. Pal, T. W. Kuo, C.-H. Hsu, D. C. Kakarla, A. Tiwari, M. C. Chou, A. Patra, P. Yanda, E. Blundo, A. Polimeni *et al.*, Interplay of lattice, spin, and dipolar properties in $CoTeMoO_6$: emergence of Griffiths-like phase, metamagnetic transition, and magnetodielectric effect, Phys. Rev. B **105**, 024420 (2022).

[10] M. Kenzelmann, A. B. Harris, S. Jonas, C. Broholm, J. Schefer, S. B. Kim, C. L. Zhang, S.-W. Cheong, O. P. Vajk, and J. W. Lynn, Magnetic Inversion Symmetry Breaking and Ferroelectricity in $TbMnO_3$, Phys. Rev. Lett. **95**, 087206 (2005).

[11] H. C. Wu, K. D. Chandrasekhar, J. K. Yuan, J. R. Huang, J.-Y. Lin, H. Berger, and H. D. Yang, Anisotropic spin-flip-induced multiferroic behavior in kagome $Cu_3Bi(SeO_3)_2O_2Cl$, Phys. Rev. B **95**, 125121 (2017).

[12] T. Aoyama, Y. Hasegawa, S. Kimura, T. Kimura, and K. Ohgushi, Anisotropic magnetodielectric effect in the honeycomb-type magnet α-RuCl$_3$, Phys. Rev. B **95**, 245104 (2017).

[13] G. Lawes, A. P. Ramirez, C. M. Varma, and M. A. Subramanian, Magnetodielectric Effects from Spin Fluctuations in Isostructural Ferromagnetic and Antiferromagnetic Systems, Phys. Rev. Lett. **91**, 257208 (2003).

[14] T. Kimura, Spiral magnets as magnetoelectrics, Annu. Rev. Mater. Res. **37**, 387 (2007).

[15] T. Kimura, Y. Sekio, H. Nakamura, T. Siegrist, and A. P. Ramirez, Cupric oxide as an induced-multiferroic with high-T_C, Nat. Mater. **7**, 291 (2008).

[16] K. Zhai, Y. Wu, S. Shen, W. Tian, H. Cao, Y. Chai, B. C. Chakoumakos, D. Shang, L. Yan, F. Wang *et al.*, Giant magnetoelectric effects achieved by tuning spin cone symmetry in Y-type hexaferrites, Nat. Commun. **8**, 519 (2017).

[17] B. K. De, V. Dwij, R. Misawa, T. Kimura, and V. G. Sathe, Femtometer atomic displacement, the root cause for multiferroic behavior of CuO unearthed through polarized Raman spectroscopy, J. Phys.: Condens. Matter **33**, 12LT01 (2021).

[18] S. F. Maehrlein, I. Radu, P. Maldonado, A. Paarmann, M. Gensch, A. M. Kalashnikova, R. V. Pisarev, M. Wolf, P. M. Oppeneer, J. Barker *et al.*, Dissecting spin-phonon equilibration in ferrimagnetic insulators by ultrafast lattice excitation, Sci. Adv. **4**, eaar5164 (2018).

[19] X. Moya and N. D. Mathur, Turn your phonon, Nat. Mater. **16**, 784 (2017).

[20] S. Ghara, E. Suard, F. Fauth, T. T. Tran, P. S. Halasyamani, A. Iyo, J. Rodríguez-Carvajal, and A. Sundaresan, Ordered aeschynite-type polar magnets RFeWO$_6$ (R = Dy, Eu, Tb, and Y): A new family of type-II multiferroics, Phys. Rev. B **95**, 224416 (2017).

[21] Y. Araki, T. Sato, Y. Fujima, N. Abe, M. Tokunaga, S. Kimura, D. Morikawa, V. Ukleev, Y. Yamasaki, C. Tabata *et al.*, Metamagnetic transitions and magnetoelectric responses in the chiral polar helimagnet Ni$_2$InSbO$_6$, Phys. Rev. B **102**, 054409 (2020).

[22] H. Watanabe, T. Kurihara, T. Kato, K. Yamaguchi, and T. Suemoto, Observation of long-lived coherent spin precession in orthoferrite ErFeO$_3$ induced by terahertz magnetic fields, Appl. Phys. Lett. **111**, 092401 (2017).

[23] V. Baltz, A. Manchon, M. Tsoi, T. Moriyama, T. Ono, and Y. Tserkovnyak, Antiferromagnetic spintronics, Rev. Mod. Phys. **90**, 015005 (2018).

[24] S. Mühlbauer, B. Binz, F. Jonietz, C. Pfleiderer, A. Rosch, A. Neubauer, R. Georgii, and P. Böni, Skyrmion lattice in a chiral magnet, Science **323**, 915 (2009).

[25] A. Modaressi, A. Courtois, R. Gerardin, B. Malaman, and C. Gleitzer, Fe$_3$PO$_7$, un cas de coordinence 5 du fer trivalent, etude structurale et magnetique, J. Solid State Chem. **47**, 245 (1983).

[26] Q. Shi, L. Zhang, M. E. Schlesinger, J. Boerio-Goates, and B. F. Woodfield, Low temperature heat capacity study of Fe$_3$PO$_7$ and Fe$_4$(P$_2$O$_7$)$_3$, J. Chem. Thermodyn. **62**, 86 (2013).

[27] K. A. Ross, M. M. Bordelon, G. Terho, and J. R. Neilson, Nanosized helical magnetic domains in strongly frustrated Fe$_3$(PO$_4$)O$_3$, Phys. Rev. B **92**, 134419 (2015).

[28] M. J. Tarne, M. M. Bordelon, S. Calder, J. R. Neilson, and K. A. Ross, Tuning the antiferromagnetic helical pitch length and nanoscale domain size in Fe$_3$(PO$_4$)O$_3$ by magnetic dilution, Phys. Rev. B **96**, 214431 (2017).

[29] C. L. Sarkis, M. J. Tarne, J. R. Neilson, H. B. Cao, E. Coldren, M. P. Gelfand, and K. A. Ross, Partial antiferromagnetic helical order in single-crystal Fe$_3$(PO$_4$)O$_3$, Phys. Rev. B **101**, 184417 (2020).

[30] A. V. Sobolev, A. A. Akulenko, I. S. Glazkova, D. A. Pankratov, and I. A. Presniakov, Modulated magnetic structure of Fe$_3$PO$_7$ as seen by ^{57}Fe Mössbauer spectroscopy, Phys. Rev. B **97**, 104415 (2018).

[31] G. Gavoille, C. Gleitzer, and G. J. Long, Etude magnétique de Fe$_3$(PO$_4$)O$_3$ avec notamment des effets de covalence et de frustation, Revue de chimie minérale **24**, 42 (1987).

[32] C. Pfleiderer, D. Reznik, L. Pintschovius, H. v. Löhneysen, M. Garst, and A. Rosch, Partial order in the non-Fermi-liquid phase of MnSi, Nature (London) **427**, 227 (2004).

[33] See Supplemental Material at http://link.aps.org/supplemental/10.1103/PhysRevB.106.094404 for additional information on SXRD, XRD, Raman, and Ga-doped FPO data.

[34] Y. S. Tang, S. M. Wang, L. Lin, C. Li, S. H. Zheng, C. F. Li, J. H. Zhang, Z. B. Yan, X. P. Jiang, and J.-M. Liu, Collinear magnetic structure and multiferroicity in the polar magnet Co$_2$Mo$_3$O$_8$, Phys. Rev. B **100**, 134112 (2019).

[35] F. Wang, T. Zou, Y. Liu, L.-Q. Yan, and Y. Sun, Persistent multiferroicity without magnetoelectric effects in CuO, J. Appl. Phys. **110**, 054106 (2011).

[36] H. C. Wu, J. K. Yuan, K. D. Chandrasekhar, C. H. Lee, W. H. Li, C. W. Wang, J. M. Chen, J.-Y. Lin, H. Berger, T. W. Yen *et al.*, Observation of charge-transfer-driven antiferroelectricity in 3d-pyrochlore multiferroic Cu$_2$OCl$_2$, Mater. Today Phys. **8**, 34 (2019).

[37] R. Saha, F. Fauth, M. Avdeev, P. Kayser, B. J. Kennedy, and A. Sundaresan, Magnetodielectric effects in A-site cation-ordered chromate spinels LiMCr$_4$O$_8$ (M = Ga and In), Phys. Rev. B **94**, 064420 (2016).

[38] L. Zhao, C.-H. Du, and A. C. Komarek, Spin-driven pyroelectricity in Ni$_3$TeO$_6$ without ferroelectric signatures of the transition at Néel temperature, Phys. Status Solidi RRL **11**, 1700073 (2017).

[39] X. Z. Lu, M. H. Whangbo, S. Dong, X. G. Gong, and H. J. Xiang, Giant Ferroelectric Polarization of CaMn$_7$O$_{12}$ Induced by a Combined Effect of Dzyaloshinskii-Moriya Interaction and Exchange Striction, Phys. Rev. Lett. **108**, 187204 (2012).

[40] C. Kittel, *Introduction to Solid State Physics*, 7th ed. (Wiley, New York, 2003).

[41] J. S. Smart and S. Greenwald, Crystal structure transitions in antiferromagnetic compounds at the Curie temperature, Phys. Rev. **82**, 113 (1951).

[42] F. J. Darnell, Temperature dependence of lattice parameters for Gd, Dy, and Ho, Phys. Rev. **130**, 1825 (1963).

[43] J. Kusz, S. Juszczyk, and J. Warczewski, An X-ray diffraction study of magnetostriction in Zn$_{1-x}$Cu$_x$Cr$_2$Se$_4$ (0.2 < x < 1.0), J. Appl. Cryst. **21**, 898 (1988).

[44] A. Nonato, B. S. Araujo, A. P. Ayala, A. P. Maciel, S. Yanez-Vilar, M. Sanchez-Andujar, M. A. Senaris-Rodriguez, and C. W. A. Paschoal, Spin-phonon and magnetostriction phenomena in CaMn$_7$O$_{12}$ helimagnet probed by Raman spectroscopy, Appl. Phys. Lett. **105**, 222902 (2014).

[45] E. Kroumova, M. I. Aroyo, J. M. Perez-Mato, A. Kirov, C. Capillas, S. Ivantchev, and H. Wondratschek, Bilbao Crystallographic Server: Useful databases and tools for phase-transition studies, Phase Trans. **76**, 155 (2003).

[46] E. Granado, A. García, J. A. Sanjurjo, C. Rettori, I. Torriani, F. Prado, R. D. Sánchez, A. Caneiro, and S. B. Oseroff, Magnetic ordering effects in the Raman spectra of La$_{1-x}$Mn$_{1-x}$O$_3$, Phys. Rev. B **60**, 11879 (1999).

[47] M. A. Prosnikov, A. N. Smirnov, V. Y. Davydov, R. V. Pisarev, N. A. Lyubochko, and S. N. Barilo, Magnetic dynamics and spin-phonon coupling in the antiferromagnet Ni$_2$NbBO$_6$, Phys. Rev. B **98**, 104404 (2018).

[48] M. N. Iliev, A. P. Litvinchuk, H.-G. Lee, C. L. Chen, M. L. Dezaneti, C. W. Chu, V. G. Ivanov, M. V. Abrashev, and V. N. Popov, Raman spectroscopy of SrRuO$_3$ near the paramagnetic-to-ferromagnetic phase transition, Phys. Rev. B **59**, 364 (1999).

[49] P. K. Pandey, R. J. Choudhary, D. K. Mishra, V. G. Sathe, and D. M. Phase, Signature of spin-phonon coupling in Sr$_2$CoO$_4$ thin film: a Raman spectroscopic study, Appl. Phys. Lett. **102**, 142401 (2013).

[50] R. D. Mero, C.-H. Lai, C.-H. Du, and H.-L. Liu, Spectroscopic signature of spin-charge-lattice coupling in CuB_2O_4, J. Phys. Chem. C **125**, 4322 (2021).

[51] C. Meyer, V. Roddatis, P. Ksoll, B. Damaschke, and V. Moshnyaga, Structure, magnetism, and spin-phonon coupling in heteroepitaxial $La_2CoMnO_6/Al_2O_3(0001)$ films, Phys. Rev. B **98**, 134433 (2018).

[52] R. Gupta, M. Kim, H. Barath, S. L. Cooper, and G. Cao, Field- and Pressure-Induced Phases in Sr_4Ru_3O: A Spectroscopic Investigation, Phys. Rev. Lett. **96**, 067004 (2006).

[53] X. K. Chen, J. C. Irwin, and J. P. Franck, Evidence for a strong spin-phonon interaction in cupric oxide, Phys. Rev. B **52**, R13130(R) (1995).

[54] A. B. Sushkov, O. Tchernyshyov, W. R. II, S. W. Cheong, and H. D. Drew, Probing Spin Correlations with Phonons in the Strongly Frustrated Magnet $ZnCr_2O_4$, Phys. Rev. Lett. **94**, 137202 (2005).

[55] H. C. Hsu, F. C. Chou, K. Koyama, K. Watanabe, and H. L. Liu, Spin-Phonon coupling in antiferromagnetic $Bi_2Sr_2CoO_{6+\delta}$: An infrared reflectance study, Phys. Rev. B **79**, 155109 (2009).

[56] U. Adem, L. Wang, D. Fausti, W. Schottenhamel, P. H. M. van Loosdrecht, A. Vasiliev, L. N. Bezmaternykh, B. Büchner, C. Hess, and R. Klingeler, Magnetodielectric and magnetoelastic coupling in $TbFe_3(BO_3)_4$, Phys. Rev. B **82**, 064406 (2010).

[57] T. Katsufuji and H. Takagi, Coupling between magnetism and dielectric properties in quantum paraelectric $EuTiO_3$, Phys. Rev. B **64**, 054415 (2001).

[58] P. T. Barton, M. C. Kemei, M. W. Gaultois, S. L. Moffitt, L. E. Darago, R. Seshadri, M. R. Suchomel, and B. C. Melot, Structural distortion below the Néel temperature in spinel $GeCo_2O_4$, Phys. Rev. B **90**, 064105 (2014).